JMES The International Journal of
Mechanical Engineering and Sciences
https://journal.its.ac.id/index.php/jmes/index
e-ISSN 2580-7471

Analysis of Pressure Distribution and Flow Patterns in a Reverse-Engineered Francis Turbine Runner Using CFD

Irwanda Yuni Pungkiarto[1], Moh. Rizanto Juliarsyah[1*], Riki Permana Sidik[2], Khoirul Anwar[1], Dhia Fairuz Shabrina[3]

[1]Department of Mechanical Engineering, Politeknik Negeri Malang, Indonesia
[2]PT PLN (Persero) Pusharlis UP2W IV, Indonesia
[3]Department of Mechanical Engineering, ITS, Sukolilo Surabaya 60111, Indonesia

Received: 22 June 2026, Revised: 4 July 2026, Accepted: 15 July 2026

Abstract

This study evaluates the hydraulic performance and steady internal-flow characteristics of an existing Francis turbine using an integrated reverse-engineering and computational fluid dynamics approach. The as-is runner geometry was obtained through multi-view three-dimensional scanning, reconstructed into a watertight computer-aided design model, and incorporated into a complete hydraulic domain comprising the spiral casing, guide vanes, runner, and draft tube. Steady-state Frozen Rotor simulations were conducted for six guide-vane openings from 4.3° to 19.3° at operating heads of 60, 100, and 136 m. A three-level grid-sensitivity assessment showed medium-to-fine differences below 2% for discharge, torque, shaft power, and hydraulic efficiency. Discharge and shaft power increased with guide-vane opening, whereas efficiency reached a head-dependent maximum before declining. The best-efficiency openings were 17.3° at 60 m, 15.3° at 100 m, and 13.3° at 136 m. The hill chart, pressure contours, streamlines, and blade-loading distributions showed that moderate openings produced more balanced hydraulic loading and better-organized mean flow. At the available comparison point, the predicted shaft power differed from the plant reference by 2.48%. This result represents engineering-level consistency rather than complete experimental validation.

Keywords: Francis turbine, reverse engineering, computational fluid dynamics, guide-vane opening, hill chart, pressure distribution.

1. Introduction

Hydropower remains an important renewable-energy source because it can provide stable power generation over long operating periods. Among hydraulic turbines, the Francis turbine is widely used in medium- and high-head power plants, where it must operate under variable head, discharge, and load conditions. These operating variations strongly affect the internal flow structure, blade loading, and overall hydraulic efficiency of the turbine [1–3].

One of the most influential operating variables in a Francis turbine is guide-vane opening. The guide vanes regulate both discharge and inlet flow angle before water enters the runner. A change in guide-vane opening therefore modifies the incidence angle at the runner inlet, the pressure difference between the pressure and suction sides of the blades, and flow direction toward the draft tube [4–7]. Because turbine performance is not represented adequately by a single operating point, efficiency must be evaluated over a range of discharge and head conditions. A hill chart is useful for this purpose because it maps turbine efficiency using unit parameters, allowing the best-efficiency region to be identified across different operating conditions [8–10].

For many existing hydropower plants, original runner design data are incomplete, unavailable, or no longer fully representative of the installed component. Long-term operation, maintenance, repair, erosion, sediment-laden flow, and local wear may cause the actual geometry to differ from the original design. In this study, the term *as-is geometry* refers to the present physical shape of the installed runner as captured by 3D scanning. This geometry is not an idealized design model; rather, it is a reconstructed representation of the actual runner surface after operational history and maintenance. Figure 1 illustrates the transition from scanned point cloud to reconstructed CAD geometry and Figure 2 shows the comparison between scanned geometry and remodeled CAD geometry.

Reverse engineering provides a route for reconstructing actual turbine geometry when design drawings are unavailable. The reconstructed geometry can then be used in CFD to estimate hydraulic performance and internal flow patterns. However, the accuracy of such a

*Corresponding author. Email: Mohammad.rizanto@polinema.ac.id, phone: +62 85156718814

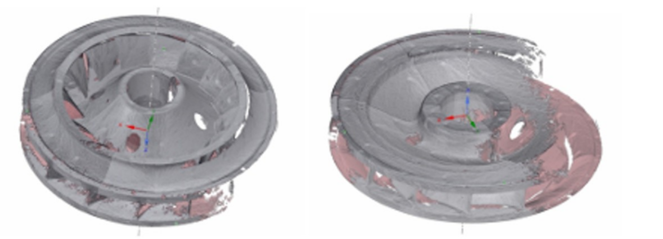

Figure 1. Scanned runner geometry obtained from 3D scanning; gray regions indicate captured surface data and red regions indicate incomplete/noisy scan areas.

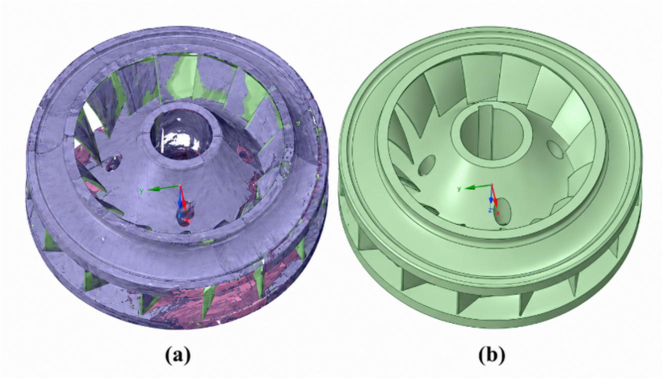

Figure 2. Comparison between (a) scanned geometry (b) remodeled CAD geometry.

workflow depends on two critical issues: the fidelity of CAD reconstruction relative to the scanned point cloud and the reproducibility of the CFD model. Smoothing and symmetrization can improve mesh quality, but they may also remove real geometric deviations. Therefore, geometric deviation assessment, mesh-quality evaluation, convergence monitoring, and careful boundary-condition definition are necessary before drawing engineering conclusions [11–13].

The research gap addressed in this paper is the limited availability of practical, reproducible assessment procedures for existing Francis turbines when only *as-is* scanned geometry and limited plant data are available. Previous studies have demonstrated the value of CFD for turbine performance analysis and the usefulness of reverse engineering for digital reconstruction; however, fewer studies combine scanned *as-is* geometry, multi-head guide-vane-opening analysis, hill-chart construction, and internal-flow interpretation within a single workflow for an operating hydropower asset. Accordingly, this work contributes: (i) an *as-is* reverse-engineering workflow for generating a CFD-ready Francis turbine model; (ii) CFD-based performance curves for six guide-vane openings at three heads; (iii) a unit-speed and unit-discharge hill chart for identifying the best-efficiency operating region; and (iv) pressure-contour and streamline-based interpretation of off-design flow behavior, with explicit limitations regarding steady-state simulation and available validation data.

Integrating a solar still with a solar thermal collector is a promising strategy to increase heat input, enhance basin water temperature, and improve distillate productivity. Therefore, this study compares three configurations: a conventional solar still (SS), a solar thermal collector (STC), and an integrated solar still–solar thermal collector system (SS+STC). The system performance was evaluated using useful heat gain, thermal efficiency, evaporation rate, and freshwater productivity under dry and rainy season conditions. The novelty of this study lies in the analytical comparison of SS, STC, and SS+STC configurations under seasonal climatic conditions using validated temperature data and integrated thermal performance indicators.

2. Theoretical method

This study used a reverse-engineering-CFD workflow to evaluate the hydraulic performance of an existing Francis turbine runner. The procedure consisted of five main stages: (1) runner digitization using 3D scanning; (2) point-cloud processing and CAD reconstruction; (3) computational-domain preparation and mesh generation; (4) steady-state CFD simulation; and (5) post-processing of performance parameters, hill-chart characteristics, pressure distribution, and streamline patterns. The method section focuses only on the numerical setup and post-processing procedures directly used to generate the reported results.

2.1. Reverse Engineering and Geometry Reconstruction

Table 1. 3D scanner specifications.

Parameter	Specification
Model	HandySCAN 700
Manufacturer	Creaform
Measurement rate	480,000 measurements/s
Resolution	0.050 mm
Accuracy	Up to 0.030 mm
Volumetric accuracy	0.020 mm + 0.060 mm/m
Stand-off distance	300 mm
Depth of field	250 mm
Output formats	.dae, .fbx, .obj, .ply, .stl, .txt, .wrl, .x3d, .x3dz, .zpr
Software	VXelements

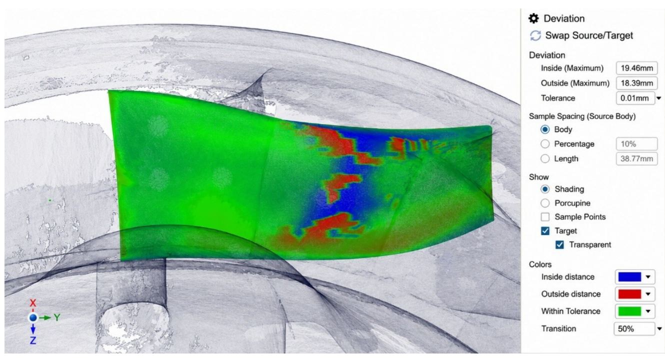

Figure 3. CAD-to-scan deviation map between the reconstructed CAD model and the scanned Francis turbine runner geometry. Green regions indicate low deviation where sufficient scanning reference data were available, while blue and red regions indicate higher inward and outward deviations caused mainly by incomplete scan coverage in areas that could not be fully reached by the 3D scanner probe.

The runner surface was captured using multi-view 3D scanning. Multiple scan angles were used to reduce occlusion around the leading edge, trailing edge, hub fillets, and shroud transition regions. The scanning process produced a point-cloud/surface mesh that was subsequently cleaned, aligned, and reconstructed into a CAD model. The scanner specification is summarized in Table 1.

The scanned data were converted into surface patches using spline/NURBS-based reconstruction. Geometric healing was then applied to remove holes, non-manifold features, and self-intersections, resulting in a watertight CAD model suitable for mesh generation and CFD simulation. Blade-to-blade periodicity and geometric symmetry were checked after reconstruction to maintain the consistency of the runner geometry. Because smoothing and symmetrization may reduce real *as-is* geometric variations, the reconstructed CAD model was compared with the scanned point cloud using CAD-to-scan deviation analysis.

The CAD-to-scan deviation map in Figure 3 shows the geometric agreement between the reconstructed CAD surface and the scanned runner surface. The green regions indicate areas with relatively low deviation, where sufficient reference surface data were obtained from the 3D scanning process. These areas were successfully captured by the scanner and therefore show better correspondence between the scanned data and the reconstructed CAD model. In contrast, the blue and red regions represent higher inward and outward deviations, respectively. These high-deviation regions mainly occur in areas where the reference surface from the scanning data was incomplete or unavailable due to limited accessibility of the 3D scanner probe, line-of-sight obstruction, and local occlusion during scanning. Therefore, the blue and red regions should not be interpreted only as actual geometric errors or physical deformation of the runner, but also as a consequence of incomplete scan coverage during the reverse engineering process.

The quantitative deviation information obtained from the available CAD-to-scan inspection output is summarized in Table 2. The maximum inward deviation was 19.46 mm, while the maximum outward deviation was 18.39 mm. These maximum values mainly represent localized deviations in regions with incomplete scan coverage.

Table 3 presents the main geometric and operating specifications of the Francis turbine used in the CFD simulation. The runner has a diameter of 764 mm and consists of 15 runner blades and 16 guide vanes. The runner inlet width is 73 mm, while the outlet diameter is 525 mm. The turbine was evaluated based on a rated head of 104 m and a rated discharge of 1.17 m^3/s. The rated or measured generator output for validation was 1050 kW, while the rotational speed was set at 750 rpm.

Table 2. CAD-to-scan deviation information of the reconstructed Francis turbine runner.

Parameter	Value	Unit/Description
Maximum inward deviation	19.46	mm
Maximum outward deviation	18.39	mm
Tolerance setting	0.01	mm

Table 3. Turbine geometry and operating parameters.

Parameter	Value
Runner diameter, D	764 mm
Number of runner blades	15
Number of guide vanes	16
Runner inlet width/outlet diameter dimensions	Inlet width: 73 mm, Outlet diameter: 525 mm
Rated head	104 m
Rated discharge	1.17 m^3/s
Rated measured generator output	1050 kW reference value at validation point
Rotational speed	750 rpm
Operating heads simulated	60 m, 100 m, and 136 m
Guide-vane openings simulated	$4.3°$, $9.3°$, $13.3°$, $15.3°$, $17.3°$, and $19.3°$
Flow passage represented	Spiral casing, guide vane, runner, and draft tube

Table 4. Grid-independence test.

Mesh	Elements	Discharge (m^3/s)	Torque (N·m)	Shaft Power (kW)	Efficiency	Relative Efficiency Difference
Coarse	950,000	1.238	13,762	1,080	0.890	2.53%
Medium	1,342,000	1.240	13,635	1,076	0.881	1.50%
Fine	6,900,000	1.242	13,465	1,057	0.868	Reference

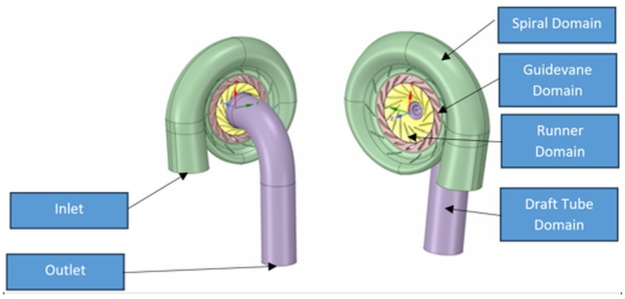

Figure 4. Francis turbine computational domain.

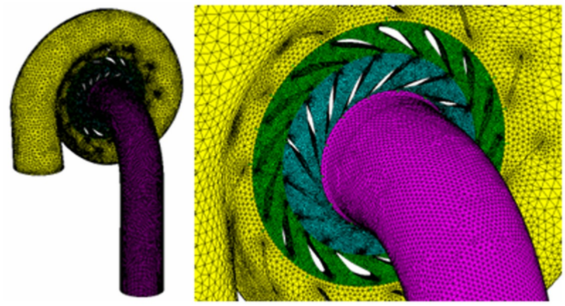

Figure 5. Computational domain mesh.

The numerical simulations were conducted under three operating heads of 60 m, 100 m, and 136 m, with six guide-vane openings of 4.3°, 9.3°, 13.3°, 15.3°, 17.3°, and 19.3°. The simulated flow passage included the spiral casing, guide vane, runner, and draft tube. Therefore, the computational domain represents the main hydraulic components required to evaluate the overall turbine performance and internal flow behavior. The inclusion of these geometric and operating parameters improves the reproducibility of the CFD model and provides a clearer basis for interpreting the performance curve, hill chart, pressure distribution, and streamline results.

2.2. Computational Domain and Mesh Generation

To assess geometric fidelity, the reconstructed CAD surface was compared with the scanned point cloud using deviation mapping. The evaluation considered mean deviation, standard deviation, and the percentage of points within the selected tolerance band, while particular attention was given to the blade leading and trailing edges because errors in these regions may affect the predicted hydraulic performance [12, 13]. Particular consideration was given to deviations along the leading edge and trailing edge of the blade, because small errors in these areas can result in large differences in predicted values of torque and pressure pulsations [12].

Figure 4 shows the computational domain used in the CFD simulation of the Francis turbine. The domain consists of four main hydraulic components: the spiral casing, guide vane, runner, and draft tube. The spiral casing functions as the inlet passage that distributes water toward the guide vane. The guide-vane domain regulates the flow direction and discharge before the water enters the runner. The runner was defined as the rotating domain where hydraulic energy is converted into mechanical energy, while the draft tube serves as the outlet passage and helps recover residual kinetic energy.

The inlet boundary was applied at the spiral casing entrance, while the outlet boundary was assigned at the end of the draft tube. The spiral casing, guide vane, and draft tube were treated as stationary domains, whereas the runner was modeled as a rotating domain. By including the complete flow passage from the spiral casing inlet to the draft-tube outlet, the computational domain provides a representative model for evaluating turbine performance, pressure distribution, and internal flow patterns.

A three-dimensional tetrahedral mesh was generated for the complete computational domain. This mesh type was selected because it can represent the complex curved geometry and narrow flow passages of the Francis turbine. Local mesh refinement was applied near the guide-vane passages, runner blade leading and trailing edges, wall regions, and runner–draft tube interface, where large velocity gradients and pressure variations were expected [3, 14]. Such local refinement is important in hydraulic turbomachinery simulations because the accuracy of predicted pressure distribution, torque, and efficiency is strongly affected by the discretization quality in regions with high flow gradients [6, 13].

Figure 5 shows the mesh distribution used in the CFD model. The final mesh consisted of 274,398 nodes and 1,342,380 elements. The spiral casing domain contained 42,305 nodes and 208,577 elements, the guide-vane domain contained 69,980 nodes and 328,246 elements, the runner domain contained 113,142 nodes and 554,885 elements, and the draft-tube domain contained 48,971

Table 5. CFD setup and boundary conditions.

Parameter	Setting
Software	ANSYS CFX 2020 R2
Simulation type	Three-dimensional steady-state
Fluid	Water, incompressible Newtonian
Water temperature	25 °C
Water density	998 kg/m^3
Dynamic viscosity	8.9×10^{-4} Pa·s
Turbulence model	k-ε
Runner rotational speed	750 rpm
Rotating domain	Runner
Stationary domains	Spiral casing, guide vane, draft tube
Rotor-stator interface	Frozen Rotor
Inlet boundary	Total pressure
Inlet total pressure	586 kPa, 978 kPa, and 1330 kPa for 60 m, 100 m, and 136 m heads
Outlet boundary	Static pressure = 0 Pa gauge at draft tube outlet
Wall boundary	No-slip wall
Inlet turbulence intensity	5%
Target residual	10^{-4}
Monitored variables	Discharge, torque, shaft power, and hydraulic efficiency

nodes and 250,672 elements. Local refinement was applied near the wall regions, guide-vane passages, runner blade leading and trailing edges, and runner–draft tube interface to better capture large velocity gradients and pressure variations in these critical regions [3, 6, 13, 14].

The mesh configuration was selected based on geometric completeness, local refinement in critical flow regions, residual convergence, and the stability of monitored hydraulic variables during the steady-state calculation. The monitored variables included discharge, torque, shaft power, and hydraulic efficiency. Therefore, the selected mesh was considered adequate for evaluating global hydraulic performance and mean-flow characteristics. However, detailed near-wall flow interpretation should be treated cautiously because the mesh was primarily designed for global performance prediction rather than high-resolution boundary-layer analysis.

The relative efficiency difference in Table 4 was calculated against the fine-grid result using $|\eta_i - \eta_{\text{fine}}| / \eta_{\text{fine}} \times 100\%$. The value decreased from 2.53% for the coarse grid to 1.50% for the medium grid. Relative to the fine grid, the medium-grid differences were 0.16% for discharge, 1.26% for torque, 1.80% for shaft power, and 1.50% for efficiency.

All four medium-to-fine differences were below 2%, while the medium grid used approximately 80.6% fewer elements than the fine grid. The medium grid was therefore selected for the eighteen production simulations as a practical compromise between numerical stability and computational cost. The coarse grid showed larger deviations in torque, shaft power, and efficiency and was not used for the final parametric study.

Efficiency decreased monotonically from 0.890 to 0.868, indicating residual discretization sensitivity. Thus, the medium grid is adequate for comparative global-performance analysis but does not demonstrate strict asymptotic convergence. A Grid Convergence Index was not calculated because the available grid-refinement ratios were strongly nonuniform.

Numerical convergence for the retained cases was assessed using an RMS residual target of 10^{-4} together with stable monitored values of discharge, torque, shaft power, and hydraulic efficiency. Residual-history files were not preserved in the archived dataset, so no reconstructed convergence plot is presented. The grid-independence results and this residual criterion jointly support the use of the medium grid for global performance trends and steady mean-flow comparisons.

2.3. CFD Setup and Boundary Conditions

The present simulations were performed using a steady-state Frozen Rotor approach. Therefore, the numerical results represent global hydraulic performance and mean-flow characteristics rather than transient flow phenomena. This approach is suitable for comparing discharge, torque, shaft power, hydraulic efficiency, and mean pressure distribution under different operating heads and guide-vane openings. However, the model does not resolve time-dependent rotor–stator interaction, pressure pulsation, vortex precession, or transient hydraulic instability. Consequently, the pressure-contour and streamline results are interpreted only as steady or time-averaged flow features. Any discussion related to flow non-uniformity, secondary-flow tendency, or off-design behavior is based on the mean-flow field and is not intended to represent directly simulated unsteady pressure fluctuation.

The complete Francis turbine domain was simulated using ANSYS CFX 2020 R2 under a three-dimensional steady-state framework. The CFD setup and boundary conditions are presented in Table 5. Water was modeled as an incompressible Newtonian fluid at 25 °C, with a density of 998 kg/m^3 and a dynamic viscosity of 8.9×10^{-4} Pa·s. The k–ε turbulence model was used because it is suitable for predicting adverse pressure-gradient flows, possible flow separation, and near-wall flow behavior in hydraulic turbomachinery applications.

The runner was defined as the rotating domain with a rotational speed of 750 rpm, while the spiral casing, guide vane, and draft tube were treated as stationary domains. The interface between the stationary domains and the rotating runner domain was modeled using the Frozen Rotor approach. This rotor–stator interface preserves the relative circumferential position between the stationary and rotating components during the steady-state calculation. Therefore, it is appropriate for evaluating global turbine performance, pressure distribution, and mean-flow characteristics under different guide-vane openings and operating heads.

A total pressure boundary condition was applied at the spiral casing inlet, with inlet total pressures of 586 kPa, 978 kPa, and 1330 kPa corresponding to operating heads of 60 m, 100 m, and 136 m, respectively. The outlet boundary was assigned at the draft tube outlet with a static pressure of 0 Pa gauge. All solid surfaces were defined using no-slip wall conditions. The inlet turbulence intensity was set to 5%. The numerical solution was considered converged when the RMS residual reached 10^{-4} and the monitored hydraulic variables, including discharge, torque, shaft power, and hydraulic efficiency, became stable.

The present simulations were performed using a steady-state Frozen Rotor approach. Therefore, the numerical results represent global hydraulic performance and mean-flow characteristics rather than transient flow phenomena. This approach is considered suitable for comparing discharge, torque, shaft power, hydraulic efficiency, and mean pressure distribution under different operating heads and guide-vane openings. However, the model does not resolve time-dependent rotor–stator interaction, pressure pulsation, vortex precession, or transient hydraulic instability. Consequently, the pressure-contour and streamline results in this study are interpreted only as steady or time-averaged flow features. Any discussion related to flow non-uniformity, secondary-flow tendency, or off-design behavior is based on the mean-flow field and is not intended to represent directly simulated unsteady pressure fluctuation. A transient URANS or LES simulation with pressure-monitoring points would be required to analyse pressure pulsation and vortex dynamics in detail.

2.4. Performance Parameters and Hill-Chart Construction

The turbine performance was evaluated using discharge, torque, shaft power, hydraulic power, and hydraulic efficiency. The runner torque was obtained from the integration of pressure and viscous forces acting on the runner blade surfaces. The shaft power was calculated from the runner torque and angular velocity using:

$$P_s = T\omega \tag{1}$$

where P_s is the shaft power (W), T is the runner torque (N·m), and ω is the angular velocity (rad/s). The angular velocity was calculated as:

$$\omega = \frac{2\pi n}{60} \tag{2}$$

where n is the runner rotational speed (rpm). The hydraulic power available at each operating condition was calculated using:

$$P_h = \rho g Q H \tag{3}$$

where P_h is the hydraulic power (W), ρ is the water density (kg/m^3), g is the gravitational acceleration (m/s^2), Q is the discharge (m^3/s), and H is the operating head (m). The hydraulic efficiency was then calculated as:

$$\eta = \frac{P_s}{P_h} = \frac{T\omega}{\rho g Q H} \tag{4}$$

where η is the hydraulic efficiency. The performance data obtained from six guide-vane openings and three operating heads were used to develop the performance curves and hill chart.

2.5. Validation and Uncertainty Assessment

The CFD prediction was compared with available plant data at one operating condition. The available reference power was 1050 kW, while the CFD simulation predicted a shaft power of 1076 kW. The percentage error was calculated as:

$$\text{Error} = \frac{|P_{s,\text{CFD}} - P_{\text{ref}}|}{P_{\text{ref}}} \times 100\%$$

$$\text{Error} = \frac{|1076 - 1050|}{1050} \times 100\% = 2.48\%$$

This comparison indicates that the CFD-predicted shaft power is close to the available plant reference value at the selected operating condition. However, because the validation is based on only one operating point, it should be interpreted as an engineering-level comparison rather than a complete experimental validation. If the reference value represents generator electrical output rather than turbine shaft power, generator efficiency and mechanical losses should be considered before direct comparison. Additional validation using several operating points, including head, discharge, power, and efficiency, would be

Table 6. Performance of Francis turbines in hydroelectric power plants based on simulation results.

Guide Vane Angle (°)	Discharge (m^3/s)	Shaft Power (kW)	Efficiency (η)
Head 60 m			
4.3	0.23	77	0.58
9.3	0.54	247	0.79
13.3	0.78	397	0.87
15.3	0.89	473	0.90
17.3	1.01	542	0.91
19.3	1.16	607	0.8977
Head 100 m			
Guide Vane Angle (°)	**Discharge (m^3/s)**	**Shaft Power (kW)**	**Efficiency (η)**
4.3	0.34	242	0.72
9.3	0.79	667	0.845
13.3	1.11	974	0.88
15.3	1.24	1076	0.881
17.3	1.357	1150	0.87
19.3	1.51	1217	0.84
Head 136 m			
Guide Vane Angle (°)	**Discharge (m^3/s)**	**Shaft Power (kW)**	**Efficiency (η)**
4.3	0.42	434	0.73
9.3	0.98	1217	0.818
13.3	1.338	1513	0.826
15.3	1.49	1661	0.82
17.3	1.61	1749	0.80
19.3	1.78	1822	0.77

required to confirm the accuracy of the model across the full operating range.

The uncertainty in this study originates mainly from two sources: geometric reconstruction and numerical simulation. Geometric uncertainty may arise from scanner accuracy, point-cloud processing, smoothing, symmetrization, and CAD reconstruction. Numerical uncertainty may arise from mesh discretization, turbulence model selection, wall treatment, rotor–stator interface treatment, and convergence behavior. These limitations should be considered when interpreting detailed pressure and streamline results.

3. Results and Discussion

3.1. CFD Performance Curve Results

Table 6 shows the turbine performance parameter values resulting from CFD simulations. The CFD simulations were performed under six guide-vane-opening conditions of 4.3°, 9.3°, 13.3°, 15.3°, 17.3°, and 19.3° with variations in heads of 60 m, 100 m, and 136 m. The discharge value through the turbine varies depending on the head and the opening angle of the guide vane.

The CFD simulations were performed for six guide-vane openings of 4.3°, 9.3°, 13.3°, 15.3°, 17.3°, and 19.3° under three operating heads of 60 m, 100 m, and 136 m. The results show that discharge increases with guide-vane opening for all operating heads. This trend occurs because a larger guide-vane opening provides a wider flow passage and allows more water to enter the runner. Shaft power also increases with increasing guide-vane opening because the hydraulic energy supplied to the runner becomes larger.

However, hydraulic efficiency does not increase continuously. At each operating head, the efficiency increases up to a certain guide-vane opening and then decreases at larger openings. At 60 m head, the highest efficiency is approximately 0.91 at 17.3°. At 100 m head, the highest efficiency is approximately 0.881 at 15.3°. At 136 m head, the highest efficiency is approximately 0.826 at 13.3°. This indicates that the best efficiency point shifts toward smaller guide-vane openings as the operating head increases.

At 100 m head and 15.3° guide-vane opening, the CFD model predicted a shaft power of 1076 kW. This value differs from the available plant reference value of 1050 kW by 2.48%. The relatively small difference suggests that the model can estimate the selected operating

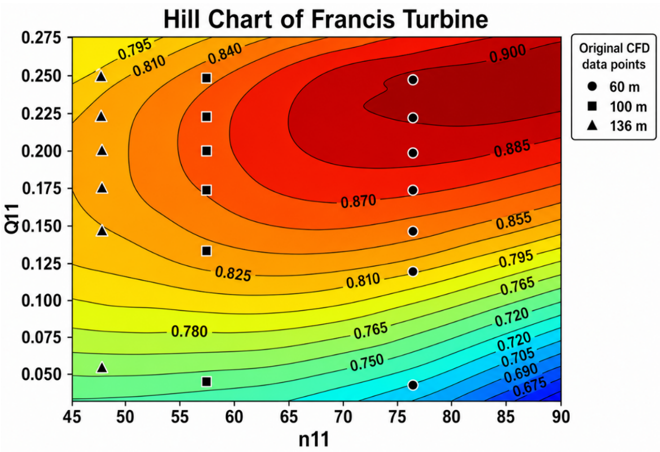

Figure 6. Hill chart of a Francis turbine hydroelectric power plant.

point reasonably well. Nevertheless, this result should not be interpreted as proof of full model accuracy for all operating conditions because only one plant reference point was available [2, 4, 15–17].

3.2. Hill Chart

A hill chart is a performance map that represents turbine efficiency over a range of operating conditions using dimensionless unit parameters. In the present study, the hill chart was constructed from the steady-state CFD results using the unit speed n_{11} and unit discharge Q_{11}, which incorporate the effects of rotational speed, discharge, runner diameter, and head into a single performance representation [8–10]. The hill chart displays efficiency contours in the form of hills, where the peaks indicate the optimal conditions for the combination of flow rate, rotational speed, and head that provide the highest efficiency. These contour lines guide turbine users in understanding how changes in flow rate and head affect turbine performance, thereby assisting in adjusting operations so that the turbine operates at maximum efficiency. This is useful for monitoring, optimizing, and planning turbine operations more efficiently. The hill chart for the Francis turbine at the hydroelectric power plant that has been studied is shown in Figure 6. The hill chart calculation formula is shown below.

$$n_{11} = \frac{nD}{\sqrt{H}} \tag{5}$$

$$Q_{11} = \frac{Q}{D^2\sqrt{H}} \tag{6}$$

where:
n_{11} = Unit value of speed
Q_{11} = Debit unit value
n = Rotational speed
D = Runner diameter
H = Turbine head

Table 7. Unit speed and unit discharge used for hill-chart construction.

Head (m)	Guide-Vane Opening (°)	Discharge (m^3/s)	Efficiency	n_{11}	Q_{11}
60	4.3	0.230	0.580	73.97	0.051
60	9.3	0.540	0.790	73.97	0.119
60	13.3	0.780	0.870	73.97	0.173
60	15.3	0.890	0.900	73.97	0.197
60	17.3	1.010	0.910	73.97	0.223
60	19.3	1.160	0.898	73.97	0.257
100	4.3	0.340	0.720	57.30	0.058
100	9.3	0.790	0.845	57.30	0.135
100	13.3	1.110	0.880	57.30	0.190
100	15.3	1.240	0.881	57.30	0.212
100	17.3	1.357	0.870	57.30	0.232
100	19.3	1.510	0.840	57.30	0.259
136	4.3	0.420	0.730	49.13	0.062
136	9.3	0.980	0.818	49.13	0.144
136	13.3	1.338	0.826	49.13	0.197
136	15.3	1.490	0.820	49.13	0.219
136	17.3	1.610	0.800	49.13	0.237
136	19.3	1.780	0.770	49.13	0.261

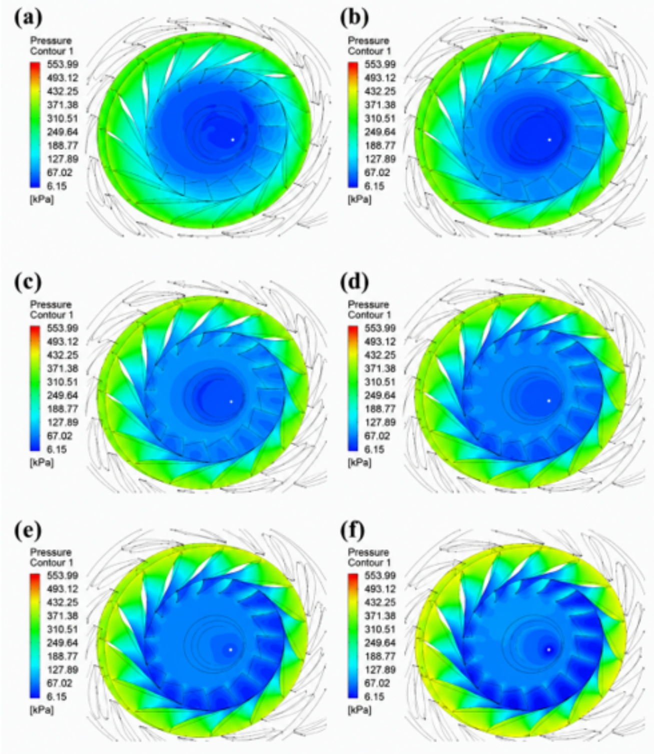

Figure 7. Pressure contours in the Francis turbine runner at an operating head of 60 m for different guide-vane opening angles: (a) $4.3°$, (b) $9.3°$, (c) $13.3°$, (d) $15.3°$, (e) $17.3°$, and (f) $19.3°$.

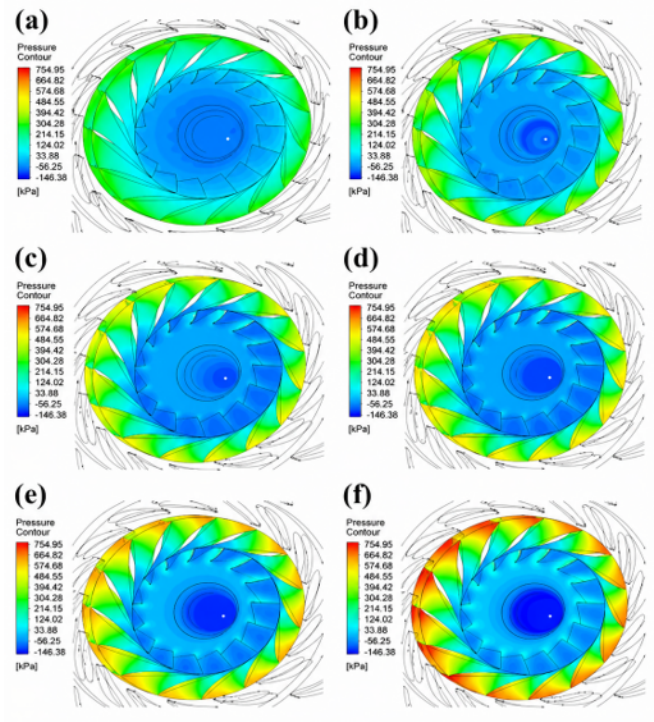

Figure 8. Pressure contours in the Francis turbine runner at an operating head of 100 m for different guide-vane opening angles: (a) $4.3°$, (b) $9.3°$, (c) $13.3°$, (d) $15.3°$, (e) $17.3°$, and (f) $19.3°$.

The hill chart was generated from 18 original CFD operating points, consisting of six guide-vane openings at each of the three operating heads. The original CFD data points were plotted directly on the hill chart as marker points, while the efficiency contours were generated using interpolation between these data points. In this study, the contour surface was produced using two-dimensional interpolation based on the calculated n_{11}, Q_{11}, and hydraulic efficiency values. Therefore, the hill chart should be interpreted as an interpolated steady-state CFD performance map rather than a complete experimentally measured turbine hill chart.

The calculated unit parameters used for hill-chart construction are summarized in Table 6. At 60 m head, the value of n_{11} was 73.97, while Q_{11} increased from 0.051 to 0.257 as the guide-vane opening increased. At 100 m head, n_{11} decreased to 57.30, while Q_{11} ranged from 0.058 to 0.259. At 136 m head, n_{11} decreased further to 49.13, while Q_{11} ranged from 0.062 to 0.261. This shows that increasing the operating head shifts the operating points toward lower unit speed values.

The hill chart indicates a high-efficiency region with efficiency values of approximately 0.885–0.900. This region represents the operating range close to the best efficiency point. The performance results show that the optimum guide-vane opening varies with head. At 60 m head, the best efficiency occurs at $17.3°$. At 100 m head, the best efficiency occurs at $15.3°$. At 136 m head, the best efficiency shifts to $13.3°$. This trend indicates that increasing the operating head changes the velocity and incidence condition at the runner inlet, so a smaller guide-vane opening is required to maintain favorable flow conditions at higher head.

Because the hill chart was generated from 18 CFD data points, the contour map should be interpreted as an interpolated performance representation. The original CFD data points should be plotted on the hill chart so that readers can clearly identify the simulated points and the interpolated regions [8–10].

3.3. Pressure Contour

Figures 7 to 9 show the water pressure contours on the runner, where the pressure gradually decreases from the inlet to the outlet of the runner. In the runner, the water pressure drops at the outlet because the water pressure is converted into mechanical torque work by the runner blades. The figures also show the pressure difference between the pressure side and the suction side of the turbine blades. This pressure difference produces a force on the runner blades and causes torque on the runner's rotating shaft.

The pressure contours show the static pressure distribution on the Francis turbine runner under different guide-vane openings and operating heads. In general, the pressure decreases from the runner inlet toward the runner outlet because part of the hydraulic energy is converted into mechanical energy by the runner. The pressure difference between the pressure side and suction side of the blade generates the blade force and runner torque. This behavior is consistent with the role of the runner and guide-vane system in directing the incoming flow and converting hydraulic energy into mechanical output [9].

At the 60 m operating head, the pressure field is relatively smoother at smaller guide-vane openings of 4.3° and 9.3°. As the guide-vane opening increases from 13.3° to 19.3°, the pressure gradient across the runner passage becomes more pronounced. This indicates stronger blade loading and less uniform pressure distribution at larger openings. Similar findings have been reported in previous CFD-based Francis turbine studies, where off-design operation and changes in guide-vane opening significantly affect internal flow structure, runner-passage behavior, and pressure distribution [18, 19]. The efficiency data support this interpretation: the efficiency increases up to 17.3° but decreases slightly at 19.3°, indicating that additional discharge beyond the best efficiency region does not produce proportional energy conversion.

At the 100 m operating head, the highest efficiency occurs at approximately 15.3° guide-vane opening. Therefore, this condition can be considered close to the best efficiency region for the 100 m head. At larger guide-vane openings of 17.3° and 19.3°, shaft power continues to increase, but efficiency decreases. This means that the additional hydraulic input is not converted into shaft power as efficiently. The pressure contour at larger openings indicates stronger pressure non-uniformity, which is consistent with off-design operation. Previous studies have also shown that guide-vane opening influences pressure and velocity distribution, vortex development, and hydraulic stability in Francis turbine flow passages [19, 20].

At the 136 m operating head, the maximum efficiency occurs at 13.3° guide-vane opening. After this point, efficiency decreases as the guide-vane opening increases. Although the shaft power increases from 1513 kW at 13.3° to 1822 kW at 19.3°, efficiency decreases from 0.826 to 0.770. This suggests that at higher head, excessive guide-vane opening may increase hydraulic loading and pressure non-uniformity. This trend is consistent with experimental and numerical studies showing that turbine performance and best-efficiency conditions vary with guide-vane opening and operating condition [20, 21]. Therefore, the pressure-contour figures are interpreted together with the quantitative CFD performance data rather than based only on visual color differences. This combined interpretation provides a clearer basis for identifying the relationship between guide-vane opening, pressure distribution, blade loading, and hydraulic efficiency. Because the present study used steady-state CFD, the pressure-contour analysis represents mean pressure distribution and should not be interpreted as evidence of transient pressure pulsation or unsteady flow instability.

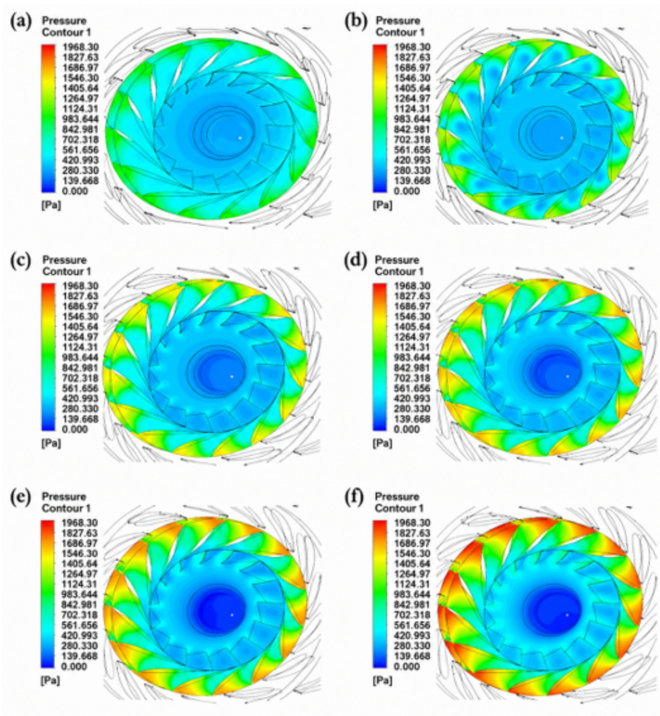

Figure 9. Pressure contours in the Francis turbine runner at an operating head of 136 m for different guide-vane opening angles: (a) $4.3°$, (b) $9.3°$, (c) $13.3°$, (d) $15.3°$, (e) $17.3°$, and (f) $19.3°$.

Table 8. Quantitative summary of pressure-contour range and corresponding best-efficiency condition.

Operating Head (m)	Approximate Pressure Range (kPa)	BEP Guide-Vane Opening	BEP Efficiency	Power at BEP (kW)	Interpretation
60	-67.77 to 553.99	17.3°	0.91	542	Moderate pressure gradient and favorable conversion near BEP.
100	-104.71 to 754.95	15.3°	0.881	1076	Higher pressure range; best efficiency occurs at a moderate opening.
136	-239.51 to 1048.20	13.3°	0.826	1513	Wider pressure range; optimum opening shifts to a smaller opening at higher head.

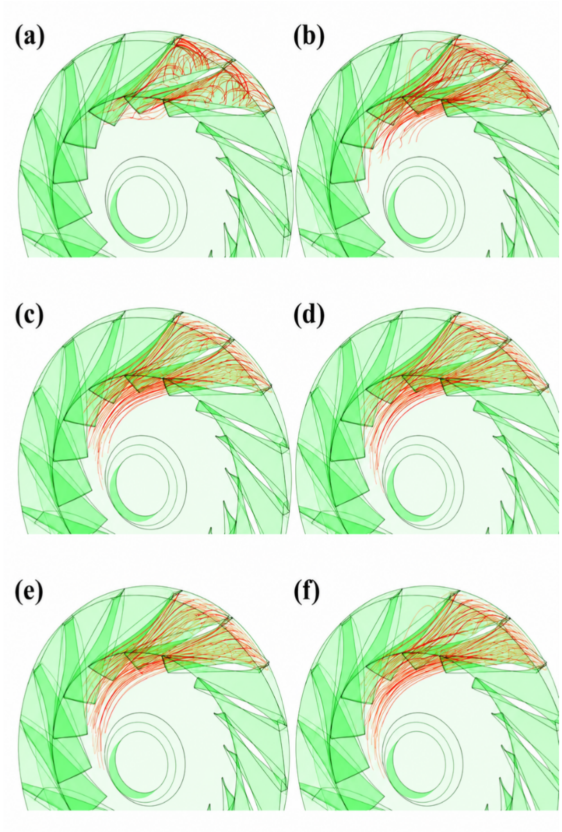

Figure 10. Streamline patterns in the Francis turbine runner at an operating head of 60 m for different guide-vane opening angles: (a) $4.3°$, (b) $9.3°$, (c) $13.3°$, (d) $15.3°$, (e) $17.3°$, and (f) $19.3°$.

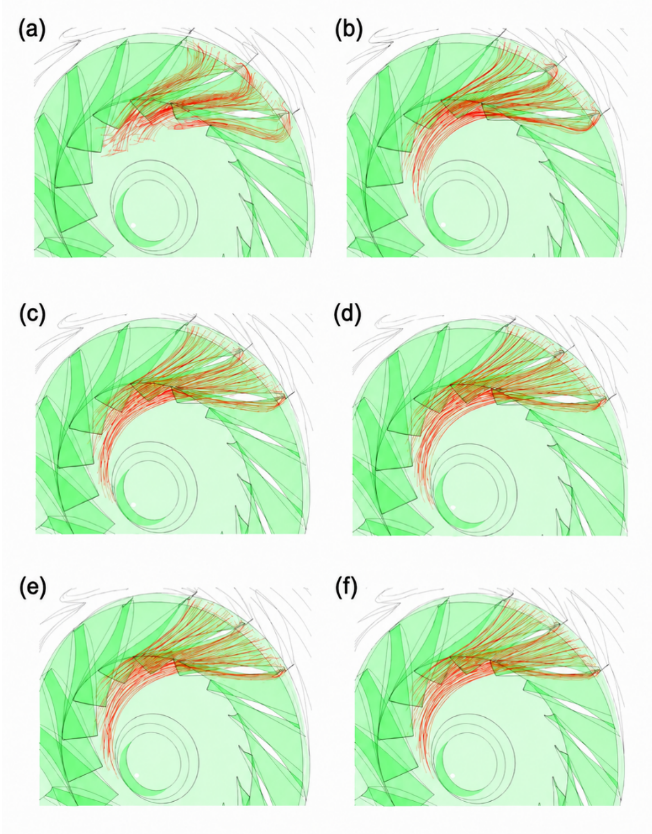

Figure 11. Streamline patterns in the Francis turbine runner at an operating head of 100 m for different guide-vane opening angles: (a) $4.3°$, (b) $9.3°$, (c) $13.3°$, (d) $15.3°$, (e) $17.3°$, and (f) $19.3°$.

To support the visual pressure-contour interpretation, the pressure range shown in the contour legends was summarized together with the corresponding best-efficiency operating condition in Table 8. The pressure range increased with operating head, from approximately -67.77 to 553.99 kPa at 60 m head, to approximately -104.71 to 754.95 kPa at 100 m head, and to approximately -239.51 to 1048.20 kPa at 136 m head. This trend is consistent with the increase in hydraulic head and blade loading.

The best-efficiency condition did not occur at the maximum guide-vane opening. Instead, it occurred at $17.3°$ for 60 m head, $15.3°$ for 100 m head, and $13.3°$ for 136 m head. This indicates that the optimum operating condition is determined not only by the magnitude of pressure difference, but also by the compatibility between inlet-flow direction, runner blade loading, and hydraulic-loss tendency. Therefore, the pressure-contour results are interpreted together with the quantitative performance data rather than from visual color distribution alone.

It should be noted that the pressure values summarized here represent the contour-legend range used for visualization. If detailed pressure-probe or area-averaged pressure data are available from post-processing, those values should be reported in place of the visualization range to provide a more rigorous quantitative assessment.

3.4. Streamline

Figures 10 to 12 present the streamline patterns within the runner passage for the three operating heads investigated in this study, namely 60 m, 100 m, and 136 m. The streamline results are used to support the interpretation of mean-flow organization obtained from the steady-state CFD simulation. Therefore, the discussion is limited to flow direction, streamline uniformity, inlet-flow compatibility with the runner blade passage, and possible hydraulic-loss tendency under different guide-vane openings.

In general, the streamline patterns show that the guide-vane opening affects how the incoming flow is directed into the runner passage. Guide-vane openings close to the best-efficiency condition produce streamlines that follow the runner passage more smoothly and uniformly. This indicates better compatibility between the inlet-flow direction and the runner blade geometry. Smaller guide-vane openings restrict discharge and underutilize the runner passage, whereas excessive guide-vane openings tend to produce more curved and less organized streamlines. This behavior suggests a higher possibility of incidence mismatch and increased hydraulic loss under off-design

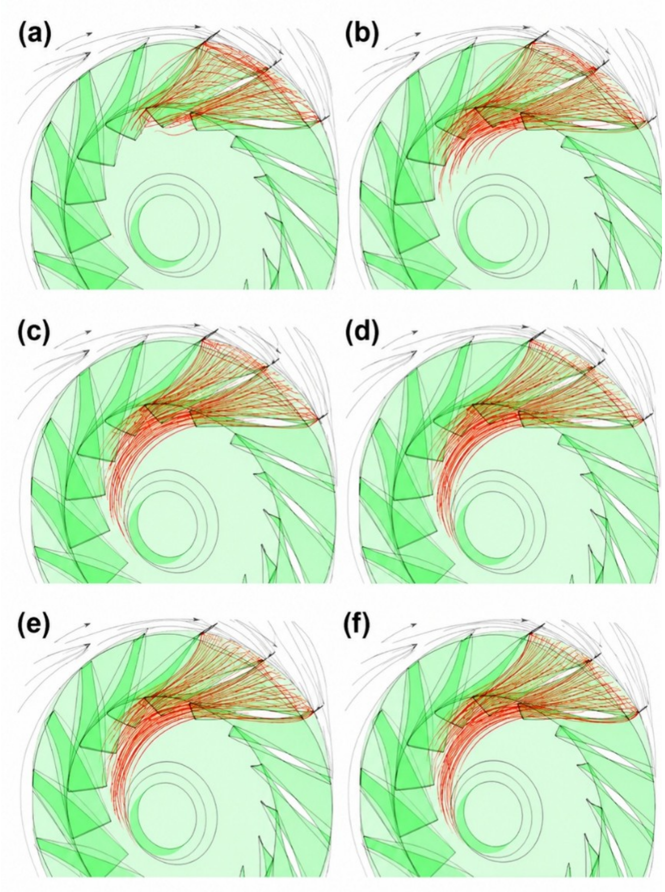

Figure 12. Streamline patterns in the Francis turbine runner at an operating head of 136 m for different guide-vane opening angles: (a) $4.3°$, (b) $9.3°$, (c) $13.3°$, (d) $15.3°$, (e) $17.3°$, and (f) $19.3°$.

mean-flow conditions.

At the 60 m operating head, the streamline distribution becomes more developed as the guide-vane opening increases. The flow pattern appears more favorable at moderate to large openings, particularly near 17.3°, where the highest efficiency for this head is obtained. When the guide-vane opening is increased further to 19.3°, the streamline arrangement becomes less uniform, which is consistent with the slight reduction in efficiency shown in the performance data. This indicates that increasing discharge beyond the best-efficiency region does not necessarily improve hydraulic energy conversion. Therefore, the 17.3° opening can be interpreted as the most favorable mean-flow condition among the simulated guide-vane openings at 60 m head [2, 4, 9].

At the 100 m operating head, the streamline pattern at 15.3° shows a relatively smoother and more organized flow structure compared with the smaller and larger guide-vane openings. This condition corresponds to the highest predicted efficiency at this head. At 17.3° and 19.3°, the shaft power continues to increase because of the larger discharge, but the efficiency decreases. The streamline visualization suggests that the additional flow may introduce greater flow non-uniformity and hydraulic loss, so the additional hydraulic input is not converted into shaft power as effectively as at the best-efficiency condition. Thus, the 15.3° opening represents the most favorable mean-flow organization for the 100 m operating head [2, 4, 9].

At the 136 m operating head, the most favorable streamline organization occurs at a smaller guide-vane opening than in the lower-head cases. The streamline pattern at 13.3° appears more compatible with the runner passage and corresponds to the highest predicted efficiency at this head. At larger guide-vane openings, the flow becomes more curved and less uniformly distributed through the runner passage. This trend indicates that, under higher-head operation, a smaller guide-vane opening is required to maintain a favorable inlet-flow condition and reduce hydraulic-loss tendency. Therefore, the 13.3° opening can be considered the most favorable mean-flow condition among the simulated guide-vane openings at 136 m head.

The streamline results are consistent with the performance data and hill-chart interpretation. The best operating condition is not obtained at the largest guide-vane opening, but at the guide-vane opening that provides the most suitable combination of discharge, inlet-flow direction, and runner blade loading. For this turbine, the best-efficiency guide-vane opening shifts from 17.3° at 60 m head to 15.3° at 100 m head and 13.3° at 136 m head. This confirms that the optimum opening decreases as the operating head increases.

Because the present CFD model was performed under steady-state conditions using a Frozen Rotor approach, the streamline results should be interpreted only as steady or time-averaged flow features. Time-dependent flow phenomena are outside the scope of the present simulation and would require transient CFD analysis or experimental measurements. Therefore, the present streamline analysis is used only to support the interpretation of mean-flow behavior and its relationship with the predicted hydraulic performance [1, 2, 15].

3.5. Flow Patterns

The water flow pattern as it passes through the draft tube is shown in Figure 13. At medium/optimum openings (around the nominal flow rate), the water flow in the draft tube is relatively parallel to the draft tube axis. Similar to secondary flow and separation in the runner, swirling flow in the draft tube also affects the flow dynamics within the draft tube, which in turn influences turbine vibration. At flow rates below 50% and above 110%, although swirling flow occurs in both cases, the direction of the swirling flow in the draft tube differs. At flow rates below 50%, the swirling flow is opposite to the direction of the runner's rotation, whereas at flow rates above 110%, the swirling flow is in the same direction as the runner's rotation.

Figure 13 shows the streamline patterns in the draft tube at an operating head of 20 m for six guide-vane openings of 4.3°, 9.3°, 13.3°, 15.3°, 17.3°, and 19.3°. The

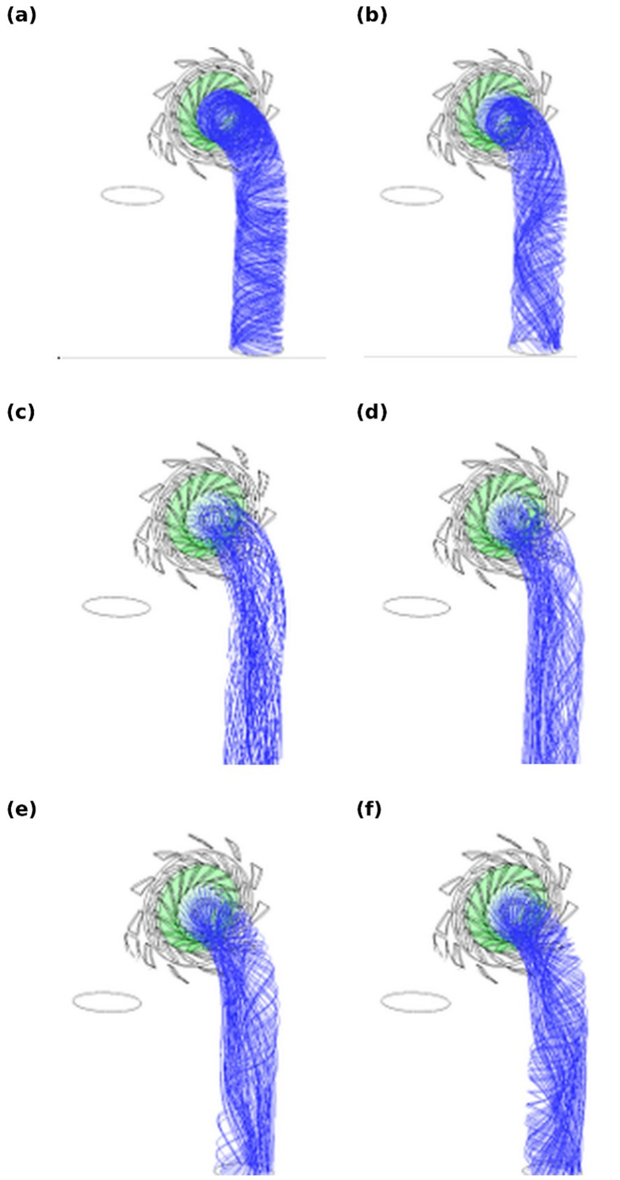

Figure 13. Steady streamline patterns in the draft tube at an operating head of 100 m for guide-vane openings of: (a) 4.3°, (b) 9.3°, (c) 13.3°, (d) 15.3°, (e) 17.3°, and (f) 19.3°.

streamline visualization indicates that the flow leaving the runner still carries a rotational component before entering the draft tube. At smaller guide-vane openings of 4.3° and 9.3°, the streamlines appear more concentrated and show stronger swirling motion near the runner outlet. This condition indicates that the flow has not yet been fully aligned with the draft-tube passage.

As the guide-vane opening increases to 13.3° and 15.3°, the flow becomes more developed and occupies a larger portion of the draft-tube passage. The streamlines show a more continuous flow path from the runner outlet toward the draft-tube exit, although some rotational motion remains visible. At larger guide-vane openings of 17.3° and 19.3°, the streamline distribution becomes more elongated along the draft tube, indicating higher discharge and stronger through-flow. However, the persistence of curved streamline patterns suggests that residual swirl and flow non-uniformity are still present.

Overall, the streamline results show that guide-vane opening affects the flow organization in the draft tube. Moderate guide-vane openings tend to produce a more stable mean-flow pattern, while very small or very large openings may increase flow non-uniformity. Because the simulation was conducted under steady-state conditions, the observed streamline patterns should be interpreted as mean-flow characteristics rather than direct evidence of transient vortex instability or pressure pulsation.

3.6. Blade Loading

The blade-loading distribution was analysed to provide a quantitative interpretation of the pressure difference between the pressure side and suction side of the runner blade. The average pressure was evaluated along the normalized streamwise position from the blade inlet to the outlet at three span locations: 0.05, 0.50, and 0.95. Since the pressure difference across the blade surface is responsible for hydraulic force and torque generation, this analysis helps explain the effect of guide-vane opening on

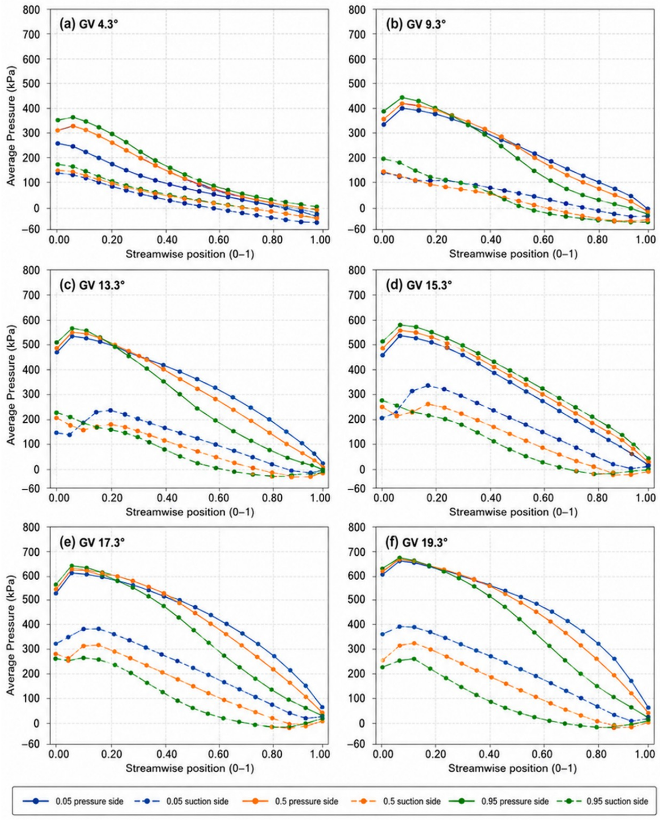

Figure 14. Average pressure distribution along the runner blade streamwise position for different guide-vane openings at an operating head of 100 m: (a) 4.3°, (b) 9.3°, (c) 13.3°, (d) 15.3°, (e) 17.3°, and (f) 19.3°. Solid lines represent the pressure side, dashed lines represent the suction side, and the blue, orange, and green curves correspond to span locations of 0.05, 0.50, and 0.95, respectively.

runner loading and turbine performance.

Figure 14 presents the blade-loading distribution of the Francis turbine runner at an operating head of 100 m under six guide-vane openings. The blade loading is represented by the average pressure distribution along the streamwise position from the blade inlet region to the blade outlet region. The results are shown for three spanwise locations, namely 0.05, 0.50, and 0.95, in which the solid lines represent the pressure side and the dashed lines represent the suction side.

In general, the pressure side shows higher average pressure than the suction side for all guide-vane openings. This pressure difference indicates the hydraulic loading acting on the runner blade and contributes to torque generation. At the smallest guide-vane opening of 4.3°, the pressure difference between the pressure and suction sides is relatively small, indicating weak blade loading and limited hydraulic energy transfer. As the guide-vane opening increases from 9.3° to 15.3°, the pressure level on the pressure side increases and the pressure difference between the pressure and suction sides becomes more pronounced. This indicates stronger blade loading and more effective energy conversion.

At the 15.3° guide-vane opening, the blade-loading distribution appears relatively smooth and well developed along the streamwise direction. The pressure decreases gradually from the inlet region toward the outlet region, showing a more stable pressure-loading pattern over the blade passage. This condition is consistent with the performance result at 100 m head, where the highest predicted efficiency occurs at the 15.3° guide-vane opening. Therefore, this opening can be interpreted as the most favorable loading condition among the simulated guide-vane openings at 100 m head.

At larger guide-vane openings of 17.3° and 19.3°, the pressure side reaches higher values, indicating stronger hydraulic loading. However, the difference between the pressure and suction sides becomes larger and less uniformly distributed, particularly in the mid-to-downstream blade region. Although these larger openings increase discharge and shaft power, the less uniform blade-loading distribution may increase hydraulic-loss tendency. This explains why the efficiency decreases at larger guide-vane openings even though the shaft power continues to increase.

Overall, the blade-loading results support the performance curve and hill-chart interpretation. The best operating condition at 100 m head is not obtained at the largest guide-vane opening, but at the opening that provides a balanced pressure difference between the pressure and suction sides, smooth pressure decay along the blade passage, and favorable hydraulic energy conversion. Based on this blade-loading analysis, the 15.3° guide-vane opening represents the most suitable operating condition for the 100 m head case.

4. Conclusions

This study evaluated the hydraulic performance of an existing Francis turbine using an integrated reverse-engineering and steady-state computational fluid dynamics approach. Eighteen operating conditions were analyzed by combining six guide-vane openings with heads of 60, 100, and 136 m. The results showed that discharge and shaft power increased with guide-vane opening, while hydraulic efficiency reached an optimum before declining. The best-efficiency openings were 17.3° at 60 m, 15.3° at 100 m, and 13.3° at 136 m, indicating that the optimum opening shifts toward a smaller angle as the operating head increases.

The pressure-contour, streamline, hill-chart, and blade-loading results showed that moderate guide-vane openings produced more balanced hydraulic loading and better-organized mean flow. The medium mesh was selected because its differences from the fine mesh were below 2% for discharge, torque, shaft power, and efficiency. At the available comparison point, the predicted shaft power was 1076 kW, differing by 2.48% from the plant reference value of 1050 kW.

These findings support the use of reverse engineering and CFD for engineering-level assessment of existing Francis turbines. However, the conclusions are limited to steady mean-flow behavior. Further studies should include validation at multiple operating points, complete geometric-deviation statistics, and transient CFD analysis to investigate pressure pulsation and unsteady flow phenomena.

References

[1] I. E. Ohiemi and A. McNabola, "Supporting the digitalisation of existing hydropower plants using computational fluid dynamics modelling," *Renewable Energy*, vol. 256, p. 124174, 2026.

[2] J. Lee, S. S. Tarannum, U. Shrestha, E. Adeeb, S. Ham, S.-J. Kim, J. Park, K.-H. Ko, Y.-D. Choi, and H.-H. Ha, "Francis turbine instabilities during off-design and transient operations: A comprehensive review of the state-of-the-art and recent research and development," *Energy Conversion and Management: X*, vol. 28, p. 101384, 2025.

[3] G. Tiwari, J. Kumar, V. Prasad, and V. K. Patel, "Utility of cfd in the design and performance analysis of hydraulic turbines—a review," *Energy Reports*, vol. 6, pp. 2410–2429, 2020.

[4] J. Pang, B. Yao, X. Liu, J. Li, M. Xiao, D. Jiang, W. Tang, L. Zhou, and Z. Lai, "Influence of guide vane opening on channel vortex and pressure pulsation in francis turbine runners," *Physics of Fluids*, vol. 36, p. 043325, 2024.

[5] Y. Hou, X. Liu, M. Xiao, H. Zhang, Y. Cai, Y. Zeng, L. Zou, and J. Pang, "Internal flow characteristics in the draft tube of a francis turbine under different working conditions," *Advances in Mechanical Engineering*, vol. 16, no. 10, 2024.

[6] S. Salehi and H. Nilsson, "Flow-induced pulsations in francis turbines during startup—a consequence of an intermittent energy system," *Renewable Energy*, vol. 188, pp. 1166–1183, 2022.

[7] M. H. Arabnejad, H. Nilsson, and R. E. Bensow, "Investigation of flow-induced instabilities in a francis turbine operating in non-cavitating and cavitating part-load conditions," *Fluids*, vol. 8, no. 2, p. 61, 2023.

[8] H.-J. Choi, M. A. Zullah, H.-W. Roh, P.-S. Ha, S.-Y. Oh, and Y.-H. Lee, "Cfd validation of performance improvement of a 500 kw francis turbine," *Renewable Energy*, vol. 54, pp. 111–123, 2013.

[9] C. Trivedi, E. Agnalt, and O. G. Dahlhaug, "Investigations of unsteady pressure loading in a francis turbine during variable-speed operation," *Renewable Energy*, vol. 113, pp. 397–410, 2017.

[10] S. Wang, L. Zhang, G. Yin, and C. Guan, "Research on unsteady hydraulic features of a francis turbine and a novel method for identifying pressure pulsation transmission path," *Water*, vol. 11, no. 6, p. 1216, 2019.

[11] J. Souček, E. Bílková, and P. Nowak, "Reverse engineering of pump as turbine for cfd analysis," *Acta Polytechnica*, vol. 64, no. 1, pp. 52–58, 2024.

[12] A. Suresh, A. Mathew, and P. B. Dhanish, "Factors influencing the measurement using 3d laser scanner: A designed experimental study," *Journal of Mechanical Science and Technology*, vol. 38, no. 10, pp. 5605–5615, 2024.

[13] S. Salehi and H. Nilsson, "Effects of uncertainties in positioning of piv plane on validation of cfd results of a high-head francis turbine model," *Renewable Energy*, vol. 193, pp. 57–75, 2022.

[14] U. Shrestha and Y.-D. Choi, "A cfd-based shape design optimization process of fixed flow passages in a francis hydro turbine," *Processes*, vol. 8, no. 11, p. 1392, 2020.

[15] A. Walid and I. Y. Pungkiarto, "Performance study of the francis turbine runner at tanggari i hydroelectric power plant via cfd and reverse engineering," *International Journal of Mechanical, Electrical and Civil Engineering*, vol. 2, no. 3, pp. 29–45, 2025.

[16] H. Sasongko and W. A. Rahman, "Numerical study of damper plate and nozzle effect on vortex turbine basin for increasing flow kinetic energy entering turbine rotor," *Journal of Mechanical Engineering, Science, and Innovation*, vol. 7, no. 1, pp. 54–63, 2023.

[17] R. A. N. Prawito, V. S. Djanali, and A. A. Wicaksono, "Numerical study of impeller trimming on a centrifugal pump test unit," *Journal of Mechanical Engineering, Science, and Innovation*, vol. 3, no. 1, pp. 8–16, 2019.

[18] C. Trivedi, E. Agnalt, and O. G. Dahlhaug, "Experimental study of a francis turbine under variable-speed and discharge conditions," *Renewable Energy*, vol. 119, pp. 447–458, 2018.

[19] Z. Zuo, S. Liu, Y. Sun, and Y. Wu, "Pressure fluctuations in the vaneless space of high-head pump-turbines: A review," *Renewable and Sustainable Energy Reviews*, vol. 41, pp. 965–974, 2015.

[20] Z. Ma and B. Zhu, "Pressure fluctuations in vaneless space of pump-turbines with large blade lean runners in the s-shaped region," *Renewable Energy*, vol. 153, pp. 1283–1295, 2020.

[21] X. Deng, H. Hua, C. Li, S. Wei, Z. Yan, W. Deng, J. Pang, Y. Xiong, L. Li, and X. Liu, "Deformation and stress of a runner in large francis turbines under wide-load operating conditions," *Water*, vol. 17, no. 16, p. 2374, 2025.